Wood Science and Technology (2025) 59:31
https://doi.org/10.1007/s00226-025-01635-9

ORIGINAL

# Multi-phase model for moisture transport in wood supported by X-ray computed tomography data

**Royson D. Dsouza[1] · Tero Harjupatana[2] · Arttu Miettinen[2] · Florian Brandstätter[3] · Anni Harju[4] · Martti Venäläinen[4] · Veikko Möttönen[5] · Marc Borrega[1,6] · Antti Paajanen[1] · Josef Füssl[3] · Stefania Fortino[1]**

Received: 19 August 2024 / Accepted: 22 January 2025 / Published online: 14 February 2025


## Abstract

This study investigates the dynamics of moisture transport in Scots pine (*Pinus sylvestris* L.) heartwood and sapwood, under alternating drying and wetting cycles, incorporating interactions between bound water, free water, and water vapor using a multi-phase model. Cylindrical specimens oriented longitudinally, radially, and tangentially were subjected to controlled relative humidity (RH) steps of 33%, 94%, and 64% at 23 °C. High-resolution X-ray computed tomography (CT) provided detailed, time-resolved measurements of moisture distributions within the wood. A multi-phase model was developed that couples Fickian diffusion (for bound water and vapor) with Darcy's law (for free water), supplemented by phase-conversion terms that account for evaporation and sorption. Key parameters, including absolute and relative permeabilities, direction-dependent vapor diffusivity reductions, thermal conductivity tensors, and free water transport formulations, were determined by matching predicted moisture profiles to the CT measurements. Among concentration and mixed concentration-pressure formulations for free water model, the mixed approach produced the most accurate match. The CT images revealed a rapid depletion of free water during the initial drying step, followed by distinct variations in bound water content as the RH was raised and lowered. Numerical simulations

✉ Royson D. Dsouza
Royson.dsouza@vtt.fi

1 VTT Technical Research Centre of Finland Ltd, Vuorimiehentie 2, 02150 Espoo, Finland

2 Department of Physics, Nanoscience Center, and School of Resource Wisdom, University of Jyväskylä, Survontie 9, 40014 Jyväskylä, Finland

3 Institute for Mechanics of Materials and Structures, TU WIEN, Karlsplatz 13, 1040 Vienna, Austria

4 Natural Resources Institute Finland, Vipusenkuja 5, 57200 Savonlinna, Finland

5 Natural Resources Institute Finland, Yliopistokatu 6 b, 80100 Joensuu, Finland

6 VTT Technical Research Centre of Finland Ltd, Tekniikantie 21, 02150 Espoo, Finland

closely replicated these trends, indicating that the calibrated model effectively represents moisture transport both above and below the fiber saturation point.

## Introduction

Engineered wood products have emerged as a cornerstone of modern construction, valued for sustainability, favourable strength-to-weight ratio, and design flexibility. Wood, as a sustainable raw material, is extensively used in construction as timber and engineered wood products, as well as in the form of wood fibers to reinforce various composites in the construction and automotive sectors (Sterley et al. 2021). The use of wood as a construction material is particularly advantageous due to its low environmental impact. Wood products can achieve high mechanical performance also at the structural level, as demonstrated by recent efforts to design and construct high timber buildings in Europe (Malo et al. 2016). However, the hygroscopic nature of wood, characterized by its anisotropic, moisture-dependent properties along the material directions, introduces substantial challenges in preserving long-term structural integrity. The moisture content (MC) of wood significantly influences its mechanical properties, including stiffness and strength, and its dimensional stability. Fluctuations in MC leads to swelling (with increased MC) and shrinkage (with decreased MC), often resulting in non-uniform dimensional changes that can induce internal stresses and potentially compromise the structural integrity of wood (Thybring et al. 2021). MC variations can induce stresses in wood components of buildings with consequent crack risk, and cupping deformations in large components such as timber decks of bridges (Fortino et al. 2019), large-span timber structures such as buildings (Dietsch and Winter 2018). Figure 1A schematically illustrates the

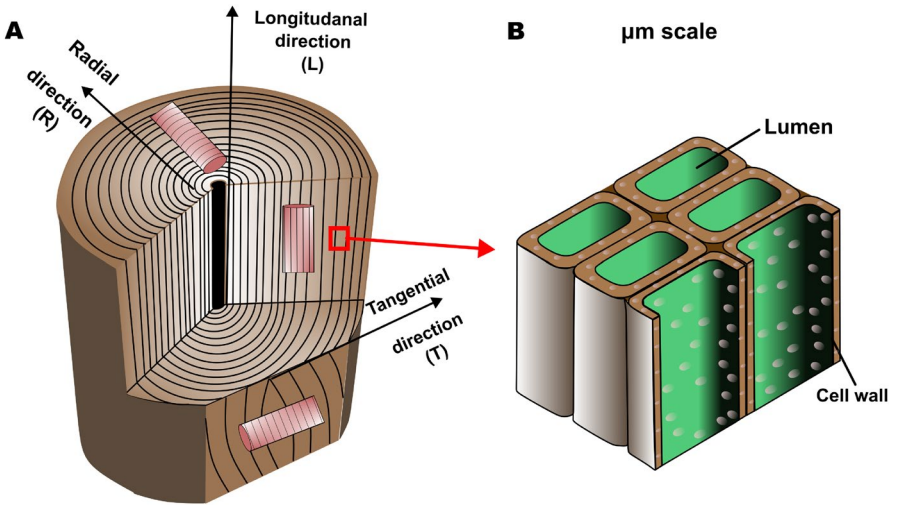


**Fig. 1** **A** Schematic representation of the three principal directions of wood with respect to grain direction and growth rings; **B** magnified view (µm scale) showing the cellular structure of wood

macroscopic structure of wood, showing the three principal directions: radial (R), tangential (T), and longitudinal (L)-critical for understanding its anisotropic behavior in moisture transport. Figure 1B presents a microscale view, revealing the porous cellular structure in which moisture resides in different states.

Within the intricate cellular structure, moisture appears in three primary states: bound water in the the cell walls, water vapor in the lumens (hollow cavities within wood cells), and free water, which occupies the lumens when MC in wood exceeds the fibre saturation point (FSP). These three phases of water that interact dynamically, continuously seeking to achieve an equilibrium moisture content (EMC). The EMC represents a state of balance between the MC in wood and the surrounding RH and temperature. The total MC is typically defined as the combined mass of bound and free water, measured against the oven-dry mass of the wood, with the mass of water vapor being negligible because of its lower density (Konopka and Kaliske 2018) i.e

$$\mathrm{MC} = \frac{\text{mass of bound water} + \text{mass of free water}}{\text{dry mass of wood}} \tag{1}$$

The FSP is a critical threshold in the moisture behaviour of wood. Below the FSP, moisture primarily exists as bound water within the cell walls. In certain conditions, wood may come into direct contact with liquid water, leading to MC levels exceeding the FSP (Glass et al. 2018). This can occur in scenarios like wood used as scaffold material in concrete construction, exposure to rainfall during outdoor storage, water leakage in buildings, or the construction process of timber-concrete composite floors. Above the FSP, the cell walls become fully saturated, and any additional moisture is present as free water.

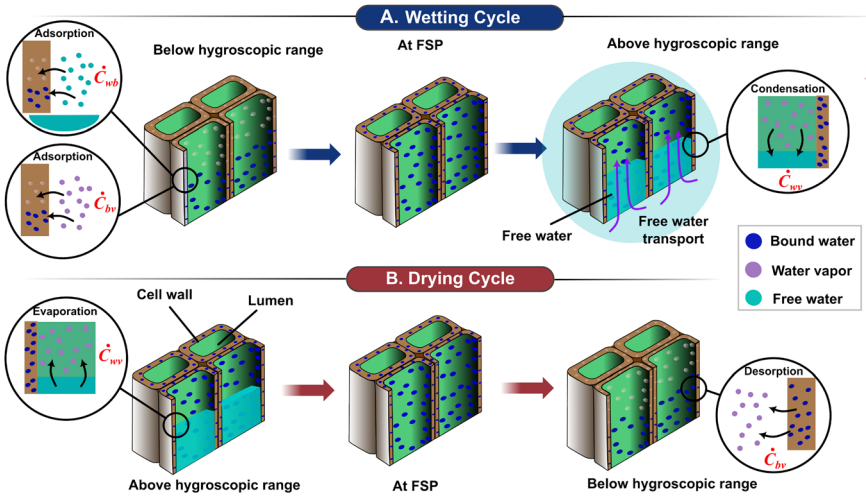


**Fig. 2** Moisture transport mechanisms during (**A**) wetting and (**B**) drying in wood, emphasizing the coupling among bound water, free water, and water vapor

Figure 2 illustrates how these three phases interact in wood during wetting and drying. During the wetting (Fig. 2A), moisture is absorbed through a combination of diffusion, capillary transport, and sorption. Vapor sorption involves the uptake of vapor by the cell walls, driven by a coupling mechanism ($\dot{c}_{bv}$) between bound water and vapor. Simultaneously, free water, which forms via capillary condensation in lumens, interacts with bound water ($\dot{c}_{wb}$) while moving into the cell walls. The process is governed by water vapor diffusion through the lumens, cell wall water diffusion, and capillary water transport, which are described separately but are typically coupled (Thybring et al. 2022). This interaction continues until equilibrium is reached, where the MC stabilizes relative to the surrounding RH and temperature. In the drying cycle (Fig. 2B), moisture is released via evaporation, desorption, and diffusion, with tightly coupled transport mechanisms dominating. Initially, free water evaporates from the wood surface, assisted by coupling between free water and vapor ($\dot{c}_{wv}$), while capillary water flow within the lumens is driven by pressure gradients. Concurrently, bound water desorbs from the cell walls and transitions to vapor phase ($\dot{c}_{bv}$). Below the FSP, bound-water diffusion predominates, with vapor diffusing through lumens as drying proceeds.

Modelling moisture transport in wood can be approached via single-phase or multi-phase formulations. Single-phase models, combine the transport mechanisms of bound water, free water, and vapor into a single governing equation to simplify the mathematical formulation (Younsi et al. 2006). While computationally efficient, single-phase models often fail to capture the distinct physical processes governing moisture transport, particularly near and above the FSP. For example, below the FSP, moisture transport is driven by bound-water diffusion and sorption, whereas above the FSP, free-water flow is influenced by capillary pressure, gravity, and evaporation. A single-phase model thus risks over-simplification, though it may suffice for relatively thin sections where gradients are small. In contrast, multi-phase models distinctly represent bound water, vapor, and free water, providing a more accurate depiction of processes under diverse moisture conditions. Below the FSP, these models account for bound water diffusion in the cell walls, sorption between bound water and vapor, and potentially sorption hysteresis (e.g., ref (Frandsen 2007; Eitelberger 2011; Fortino et al. 2013; Konopka and Kaliske 2018; Krabbenhoft and Damkilde 2004)). Above the FSP, capillary flow, bound-free water exchange, and evaporative or condensative interactions take place (Autengruber et al. 2020; Brandstätter et al. 2023), described by nonlinear coupled equations. Such detailed model demands parameterization and better identification of the transport parameters (Autengruber et al. 2020), making it non-trivial to measure all properties needed.

The multi-Fickian model, describes the simultaneous diffusion of bound water and vapor in wood as a function of concentration gradients and diffusion coefficients. It is particularly applicable to thicker wood specimens and higher RH levels, as typically encountered during the drying of wood. However, its applicability is limited to MCs below the FSP, as it does not account for the presence of free water. Frandsen et al. (Frandsen et al. 2007a) revised this model to describe non-Fickian effects in wood, focusing on the sorption rate function and boundary conditions. The model was further refined by Frandsen and Svensson (Frandsen et al. 2007b) to

incorporate sorption hysteresis, a phenomenon where the EMC depends on the history of RH variations.

The need remains for the application of comprehensive model that spans the full moisture range, including liquid water transport. Applications where wood is in contact with liquid water or high-humidity environments-such as construction sites or extended outdoor exposure-require tracking of these processes. Moreover, experimental data capturing spatio-temporal moisture distributions in wood are scarce. To obtain such data, there are only a few suitable imaging techniques available, namely neutron imaging (and tomography), nuclear magnetic resonance (NMR) imaging and X-ray computed tomography (CT).

Neutrons are sensitive to water, but the small number of neutron imaging facilities worldwide and high imaging costs for extensive measurement periods are obvious limitations (Lehmann 2017). Sensitivity to water and good availability of equipment have made NMR imaging a widely used method for studying moisture distributions in wood (Almeida et al. 2007; MacMillan et al. 2011; Žlahtič Zupanc et al. 2019). Although the spatial resolution of NMR imaging is too low (typically near 70 µm) to resolve the microstructure of wood, it is capable of quantifying bound and free water through spin relaxation time analysis (Cai et al. 2020). However, the typical sample size of tens of millimetres, required for sufficient NMR signal, leads to moisture transport experiments lasting up to several months, if not a year (Dvinskikh et al. 2011; Gezici-Koç et al. 2017). Measuring an extensive set of experiments may thus be impractical due to time constraints.

X-ray tomography produces high-resolution (down to 1 µm) volume images of samples and is thus an efficient tool for studying the microstructure of many heterogeneous materials (Landis and Keane 2010). Laboratory-scale microtomography devices are relatively common in many research institutes and companies nowadays. Although X-rays are not so sensitive to water compared to neutrons and NMR, CT is still capable of monitoring the water transport in many materials. However, for swelling materials (such as wood) non-standard calibration and correction methods are needed to enable quantitative water content analysis (Harjupatana et al. 2015; Miettinen et al. 2016). As CT allows to use smaller samples while still producing high-quality data, the sample size was decreased to a few millimeters. This reduced the duration of a single moisture transport experiment to a few weeks, which is convenient as an extensive set of wood samples can be measured in a relatively short time.

In the present work, X-ray CT is used to track free and bound water distributions in Scots pine samples subjected to alternate drying and wetting cycles. The resulting CT data is used to inform and calibrate multi-phase models, derived from previous approaches for MC below-FSP (Fortino et al. 2019) and above-FSP free-water flow (Autengruber et al. 2020). This allows for the explicit incorporation of both bound and free water transport mechanisms, with a time-dependent evaporation rate that simulates the transition between free water and water vapor during the drying process. The model accounts for the diffusion of bound water within the cell walls, driven by concentration gradients, and the capillary flow of free water through the lumens, influenced by pressure gradients. Additionally, the model considers the evaporation of free water from the wood surface, a function

of the surrounding environment's RH and temperature. Transport parameters (e.g., anisotropic permeabilities, vapor-diffusivity reduction factors, thermal conductivity tensors) are fine-tuned to match the measured spatio-temporal moisture distributions, enabling an accurate simulation of how water transitions from free to bound phases, or from water to vapor. X-ray CT data also provides clear and accurate data on separate phases of the moisture content in the wood including the initial and boundary conditions.

The numerical approach presented here quantifies how free water rapidly exits lumens in early drying, while bound-water desorption and reabsorption follow slower kinetics, particularly when RH changes. Cylindrical samples oriented in L, R and T-directions, highlight wood's anisotropy and confirm the importance of accurate flow and sorption modelling in each principal direction. Different formulations for free-water transport (concentration-based vs. mixed concentration-pressure) are tested to identify the most reliable approach. Ultimately, our aim is to present a more comprehensive description of moisture transport across the FSP in Scots pine, demonstrating how high-resolution CT provides the necessary data to fine-tune multiphase moisture transport models.

## Materials and methods

### Selection and cutting of the sample tree

A Scots pine tree from a naturally regenerated stand in Mäkrä, Kerimäki, Finland (N 61°50', E 29°23') was harvested on 29$^{th}$ Nov 2022. The stand belongs to the EVOLTREE network of intensive study sites, ISS (http://www.evoltree.eu/index.php/intensive-study-sites/map). The selection of this tree was based on previous investigations initiated in 2011 (unpublished data) and 2018 (Belt et al. 2021), which emphasized stilbene and resin acid content in the outer heartwood. An average tree was chosen among several candidates. The pine's cross-measured diameter at 1.3 m height was 290 x 272 mm (excluding bark), with 54 annual rings. The heartwood diameter was 150 x 140 mm, comprising 21 annual rings. The butt log up to 3 m height was cut into approximately 30 cm long blocks and stored at −20 °C until further processing.

### Sample preparation

The wood samples were prepared from Scots pine because of its homogeneous structure and widespread use in construction applications. To ensure uniformity and minimize variability in the moisture transport properties, the samples were carefully selected, ensuring consistent density, growth ring orientation, and the absence of defects such as knots or cracks. Heartwood (HW) and sapwood (SW) samples were initially prepared and tested in all directions; however, HW samples in the T and R-directions and SW samples in the L-direction were chosen because they provided optimal results during microCT scanning, avoiding issues such as imaging artifacts, or processing errors.

One 30 cm long block was selected for preparing the cylinders. First a rectangular piece of approximately $10 \times 80 \times 150$ mm$^3$ was sawn separately from SW and HW sections of the block using a band saw. The pieces were dried at room temperature for 3–4 weeks until their weight was stabilized. Cylindrical wood samples, measuring 3 mm in diameter and 5 mm in length (see Fig. 3B), were carefully machined. These dimensions were chosen to balance the need for sufficient resolution in the X-ray CT scans with the requirement for a representative volume of wood tissue. The samples were oriented to obtain three orthogonal directions: L-direction, aligned with the grain direction; R-direction, perpendicular to the growth rings; and T-direction, tangent to the growth rings (For visual representation, see Fig. 1B). Special care was taken during the grinding process to ensure the accurate alignment of the R and T-direction orientations, as these directions exhibit distinct anatomical features and moisture transport properties.

Prior to the experiments, the lateral surfaces of the samples were sealed with polyolefin heat shrink tubes and the top surfaces with poly(methyl methacrylate) (PMMA) plugs (see Fig. 3A). This sealing ensured that the moisture transport was effectively one-dimensional in the axial direction and the moisture was transported only through the bottom surface. Such a simple and well-defined experimental geometry enabled efficient utilisation of the results in modelling.

To establish a high initial MC exceeding the FSP, the samples were submerged in distilled water for a period of 1–2 weeks. This extended submersion period guaranteed that the cell walls were fully saturated with bound water, and the lumens were filled with free water. The use of distilled water minimized the potential for contamination or chemical interactions that could influence the swelling and moisture transport behaviour.

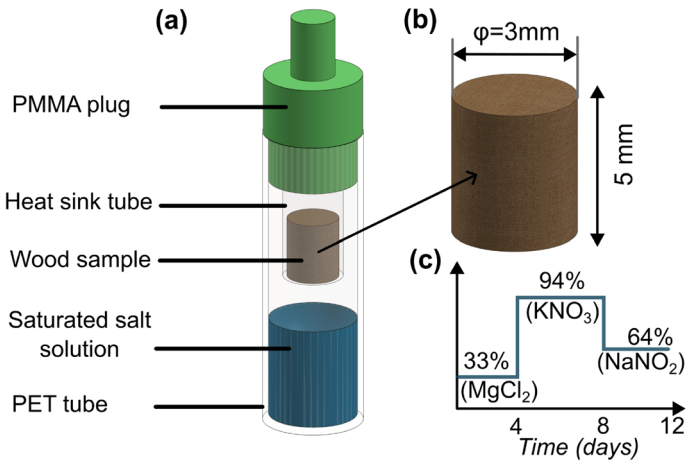


**Fig. 3** **a)** Schematic figure of the experimental setup; **b)** dimensions of the wood sample under test; **c)** RH profiles as a function of time obtained using different saturated salt solutions

### Moisture transport experiments

The prepared wood samples were carefully positioned in custom-designed sample tubes, where the bottom ends of the samples were exposed to the specific RH, generated by a saturated salt solution in the tube placed below the sample. The samples were kept inside the sample tubes during the whole experiments (also during CT scans), except for temporary removal when the RH was changed by changing the saturated salt solution. The experimental design incorporated three distinct RH steps (see Fig. 3C), strategically chosen to simulate a range of drying and wetting conditions and to comprehensively investigate the moisture transport behaviour within the wood samples.

During each RH step, X-Ray CT imaging was performed at eight designated time points: 0 h, 1.5 h, 3 h, 6 h, 12 h, 1 day, 2 days, 4 days, and extended further if necessary to capture the complete moisture transport process. These time points were selected to provide a detailed temporal resolution of the moisture distribution evolution within the samples. To obtain a well-defined reference state for the CT method, each sample was also imaged in the dry state after the experiments (oven drying at 60 °C for 24 h).

Each wood sample was weighed five times: in the fully saturated state before the experiment, at the end of each RH step (three times) and in the dry state after the experiment. These measurements gave the mass of wood and water in the samples and were used for accurate calibration of the X-Ray CT method.

### X-ray computed tomography

A Jtomo X-ray microtomography scanner (in-house built at the University of Jyväskylä) was employed to visualize and quantify the internal moisture distribution within the wood samples at high spatial resolution of 7 µm (Fig. 4). The X-ray tube was operated at 40 kV and 200 µA, and no filter was used. For each scan, a total of 721 projections, with an exposure time of 2000 ms each, were acquired resulting in a scan duration of 24 min. Such a scan time, shorter than typical, ensured that no

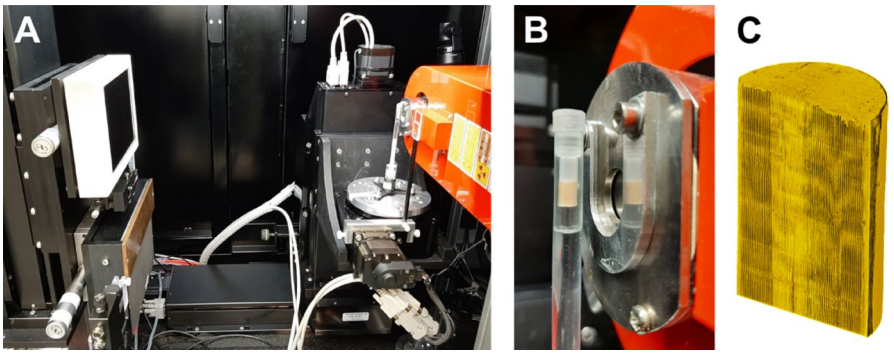


**Fig. 4** **A** Interior view of Jtomo microtomography scanner; **B** zoomed view of sample tube; and **C** 3D visualization of wood sample

significant motion artefacts appeared during the drying and wetting, while the image quality was still good enough for the data analysis. The heating of the sample by X-rays was estimated to be negligible (0.03 mW).

Each sample tube was securely positioned on the rotation stage of the CT scanner to minimize movement during scanning. The scanner captured a series of 2D projection images while the sample was continuously rotated over 360 degrees. Before and after each scan, reference X-ray images of three different thicknesses PMMA plates (1 mm, 2 mm and 3 mm) were taken. These images were used to correct beam hardening and its spatiotemporal variations from the projection images using a technique by (Harjupatana et al. 2022). The corrected projections were then reconstructed into 3D volumes using a filtered back-projection algorithm. The CT method used in this study is based on the work by (Harjupatana et al. 2015). It is assumed that voxel values of CT images obey a linear relationship

$$g(\mathbf{x}) = g_0 + \alpha_s \cdot \rho_s(\mathbf{x}) + \alpha_w \cdot \rho_w(\mathbf{x}) \tag{2}$$

where $\rho_s$ and $\rho_w$ are the partial densities of solid and water in a sample. Here the constant $g_0$ was readily known (voxel value of air) and the coefficients $\alpha_s$ and $\alpha_w$ were determined by a calibration fit to the five data points $(\bar{\rho}_s, \bar{\rho}_w, \bar{g})$ obtained from the weighings and CT images (the overlines denote the average values over the entire sample). By using Eq. (2), the partial density distribution of solid was calculated in the dry state ($\rho_w = 0$), which was chosen to be the reference state.

The deformation of the sample between the reference state and each deformed state was measured using a phase correlation-based block-matching algorithm (Miettinen et al. 2019). First, a three-dimensional rectangular grid of points with spacing 50 px, covering the entire sample, was formed in the reference state. At each grid point $\mathbf{x}$, a three-dimensional rectangular block $B_{\mathrm{ref}}(\mathbf{x})$ of radius 30 px was extracted from the reference state image, and thereafter a block $B_{\mathrm{def}}(\mathbf{x} + \mathbf{u}_0)$ of similar size was extracted from the deformed state image. The initial guess for the displacement ($\mathbf{u}_0$) was obtained by measuring the shape of the sample in the reference and deformed states using an interface detection algorithm by (Turpeinen et al. 2015) and assuming affine deformation between the states. The phase-correlogram was calculated as

$$R = \mathcal{F}^{-1}\left\{\mathcal{F}\left\{B_{\mathrm{ref}}\right\}^* \cdot \mathcal{F}\{B_{\mathrm{def}}\} / \left(\left|\mathcal{F}\left\{B_{\mathrm{ref}}\right\}^* \cdot \mathcal{F}\{B_{\mathrm{def}}\}\right|\right)\right\} \tag{3}$$

where $\mathcal{F}$ and $\mathcal{F}^{-1}$ denote forward and inverse Fourier transforms, and the asterisks (*) denote complex conjugates. Finally, the displacement at each grid point was calculated as $\mathbf{u} = \mathbf{u}_0 + \arg\ \max\ R(\mathbf{x})$, and subpixel accuracy was achieved by utilizing a quadratic polynomial fitted to the peak in the phase-correlogram.

The obtained three-dimensional displacement fields $\mathbf{u}$ were used to calculate the partial density distributions of solid in each deformed state as

$$\rho_s(\mathbf{x}) = \rho_{s,\mathrm{ref}}(\mathbf{x}) / (1 + \nabla \cdot \mathbf{u}(\mathbf{x})) \tag{4}$$

The partial density distribution of water was calculated from Eq. (2) as

$$\rho_w(\mathbf{x}) = \left(g(\mathbf{x}+\mathbf{u}) - \ g_0 - \alpha_s \cdot \rho_s(\mathbf{x})\right)/\alpha_w \tag{5}$$

The obtained partial density distributions were further used to calculate the MC distribution as $MC^{CT} = \rho_w/\rho_s$. To distinguish between bound and free water, it was assumed that all the water below the FSP is bound and the excess water above the FSP is free.

### Dynamic vapor sorption (DVS) experiments

The sorption isotherms of pine SW and HW samples were determined in a DVS Resolution system (Surface Measurement Systems, UK), using small wooden cubes with approximate dimensions of $3 \times 3 \times 3$ mm$^3$ and about 10 mg mass. The samples, stored in water to prevent drying and maintain their green state, were placed in the microbalance of the DVS apparatus. The RH was then stepwise decreased from 95% to 0% at a constant temperature of 25°C. In each step, the RH was kept constant until the change in mass of the sample over a 10 min period was lower than 0.002%. Additionally, a 2 h stabilization period was applied before decreasing the RH to the next step. The same procedure was applied for the full sorption cycle, which included both desorption and absorption, and two sorption cycles were performed for each sample. The samples were run in duplicate, and data from the second sorption cycle were used to fit the sorption models.

### Mathematical model

In this work, the mathematical model for moisture transport in wood is adapted from Fortino et al. (2019) for conditions below the FSP and Autengruber et al. (2010) for conditions above the FSP (Fortino et al. 2019; Autengruber et al. 2020). Key components of the model are summarized below, while Electronic Supplementary Material (ESM) A presents the detailed equations and numerical constants. Minor modifications to the formulations were introduced to ensure accurate simulation in comparison with the CT measurements described in this study.

The model accounts for three water phases in wood: bound water within the cell walls, water vapor in the lumens, and free water in lumens, along with the interactions between these phases. Throughout this work, tensors are represented in bold uppercase letters (e.g., **A**, **D**), vectors in bold lowercase letters (e.g., **v**, **u**), and scalars in italic lowercase letters (e.g., $x$, $y$).

Fundamental assumptions validated by previous studies include local thermal equilibrium in a representative volume element (RVE), implying that all water phases share the same temperature (Stanish et al. 1986; Perré 2015). This assumption is justified by the relatively slow rate of heat transfer in wood compared to moisture transport. The gaseous mixture in wood lumens is treated as an ideal gas, valid for the moderate temperature range considered in this study (Turner 1996). Due to the high permeability of wood to gases, the influence of dry air on moisture transport is considered negligible (Perré and Turner 1999). Convective transport of

water vapor is assumed insignificant compared to diffusive transport below 323 K (Pang 1998), and instantaneous saturation of water vapor occurs in the lumens when free water is present. Additionally, the cell wall is considered rigid in this framework, thereby neglecting any mechanical deformation or swelling.

Under these assumptions, the mass and energy conservation equations within the RVE can be formulated as a coupled system of partial differential equations:

***Conservation of bound water:***

$$\frac{\partial c_b}{\partial t} = -\nabla \cdot \mathbf{J_b} + \dot{c}_{bv} + \dot{c}_{wb} \tag{6}$$

***Conservation of water vapor:***

$$\frac{\partial (c_v f_{\mathrm{lum_{gas}}})}{\partial t} = -\nabla \cdot (\mathbf{J_v} f_{\mathrm{lum_{gas}}}) - \dot{c}_{bv} + \dot{c}_{wv} \tag{7}$$

***Conservation of free water:***

$$\frac{\partial c_w}{\partial t} = -\nabla \cdot \mathbf{J_w} - \dot{c}_{wb} - \dot{c}_{wv} \tag{8}$$

***Conservation of energy:***

$$\begin{aligned} \frac{\partial \rho h}{\partial t} = &- \nabla \cdot \mathbf{f} - \nabla \cdot \mathbf{J_b}\, \bar{h}_b - \nabla \cdot \mathbf{J_v}\, h_v f_{\mathrm{lum_{gas}}} - \nabla \cdot \mathbf{J_w}\, h_w \\ &+ \dot{c}_{bv}(h_v - h_b) + \dot{c}_{wb}(h_w - h_b) + \dot{c}_{wv}(h_w - h_v) \end{aligned} \tag{9}$$

These equations describe the evolution of concentrations and energy within the wood structure. These equations represent the fundamental principles governing the transport of moisture and energy in wood. Equation (6) describes the change in bound water concentration over time due to diffusion and sorption processes. Equation (7) describes the change in water vapor concentration due to diffusion, sorption, and the volume fraction of the lumen filled with gas. Equation (8) describes the change in free water concentration due to capillary flow and sorption. Equation (9) describes the change in total energy due to heat flux and the transport of moisture in its various phases.

The terms in these equations have the following meanings:

- $\mathbf{J_b}$, $\mathbf{J_v}$, and $\mathbf{J_w}$ represent the fluxes of bound water, water vapor, and free water, respectively.
- $c_b$, $c_v$, and $c_w$ denote the concentrations of bound water, water vapor, and free water, respectively.
- $\dot{c}_{bv}$, $\dot{c}_{wb}$, and $\dot{c}_{wv}$ represent the sorption rates between the different phases of water.
- $h_b$, $h_v$, and $h_w$ denote the enthalpies of bound water, water vapor, and free water, respectively.
- $f_{\mathrm{lum_{gas}}}$ represents the volume fraction of the lumen filled with gas.
- $\mathbf{f}$ is the heat flux.

- $\rho$ is the density of the wood.

The interaction between different water phases are governed by sorption rates $\dot{c}_{bv}$, $\dot{c}_{wb}$, and $\dot{c}_{wv}$, measured in kg/(m$^3\cdot$ s). These rates describe the mass exchange between different water phases and are formulated as:

$$\begin{aligned} \dot{c}_{bv} &= H_{bv}(c_{b,eq} - c_b) \\ \dot{c}_{wv} &= H_{wv}(c_{v,sat} - c_v) f_{\mathrm{lum}_{\mathrm{gas}}} \\ \dot{c}_{wb} &= H_{wb}(c_{b,eq} - c_b) \end{aligned} \tag{10}$$

where $H_{bv}$, $H_{wv}$, and $H_{wb}$ are non-linear reaction functions that depend on relative humidity and moisture content. The term $c_{b,eq}$ represents the equilibrium bound water concentration, and $c_{v,sat}$ is the saturated vapor concentration.

The transport mechanisms for each phase follow distinct physical principles. Bound water transport through cell walls follows Fickian diffusion with thermal gradient influence (Frandsen 2007):

$$\mathbf{J_b} = -\mathbf{D_b} \cdot \nabla c_b - \mathbf{D_{bT}} \cdot \nabla T \tag{11}$$

where $\mathbf{D_b}$ is the bound water diffusion tensor and $\mathbf{D_{bT}}$ represents the thermal diffusion tensor.

The bound water diffusion tensor $\mathbf{D_b}$ exhibits temperature dependence given by:

$$\mathbf{D_b} = \mathbf{D_0} \exp\left(\frac{-E_b}{RT}\right) \tag{12}$$

where R = 8.314 J/(mol K)

Activation energy ($E_b$) is given by:

$$E_b = \left(38.5 - 29.0 \cdot \frac{c_b}{\rho_d}\right) \cdot 10^3 \tag{13}$$

where $\rho_d$ is the dry density of the wood obtained using experimental CT data and R = 8.314 J/(mol K) The steady state diffusion coefficients are given in ESM A.

Water vapor flux is given by:

$$\mathbf{J_v} = -\mathbf{D_v} \cdot \nabla c_v \tag{14}$$

with $\mathbf{D_v}$ incorporating a direction-dependent reduction factor $\xi$ that reflects wood's cellular structure (Konopka and Kaliske 2018; Krabbenhoft and Damkilde 2004):

$$\mathbf{D_v} = \xi\left(2.31 \times 10^{-5} \frac{p_{\mathrm{atm}}}{p_{\mathrm{atm}} + p_{v_{\mathrm{air}}}} \left(\frac{T}{273}\right)^{1.81}\right) \tag{15}$$

where $p_{\mathrm{atm}}$ is the atmospheric pressure and $p_{v_{\mathrm{air}}}$ is the vapor pressure. $\xi$-factor varies with the wood's anatomical direction, reflecting the anisotropic nature of the cellular structure.

Free water movement is handled by Darcy's law:

$$\mathbf{J_w} = -\rho_{\mathrm{H_2O}} \frac{\mathbf{K_r} \cdot \mathbf{K_w}}{\mu_w} \cdot \nabla(P_g - P_c) \tag{16}$$

where $\rho_{\mathrm{H_2O}}$ is the density of water, $\mathbf{K_r}$ and $\mathbf{K_w}$ are the relative and absolute permeability tensors respectively, $\mu_w$ is the dynamic viscosity of water, and $P_g - P_c$ represents the difference between gaseous and capillary pressures. For the liquid permeability tensors, initial values from previous publications are used and further calibrated to fit the CT data.

Initial conditions are established to reflect realistic moisture states in wood. The initial free water concentration is determined through CT measurements, providing spatial distribution of moisture above FSP. The initial water vapor concentration, $c_{v,\mathrm{ini}}$, is set to the saturated vapor concentration, $c_{v_{\mathrm{sat}}}$, which is estimated based on the initial RH conditions.The initial bound water concentration, $c_{b,\mathrm{ini}}$, is chosen to be in equilibrium with $c_{v,\mathrm{ini}}$. The mathematical details of these equilibrium relationships and their temperature dependence are provided in ESM A.

In this model (based on the experimental setup), no free water at the boundary surface is considered. In this case, the free water flux ($\phi_w$) is zero, and only the water vapor flux ($\phi_v$) needs to be considered. The water vapor flux is modeled using a convective boundary condition More details on boundary conditions, including the coupling terms and parameters, are detailed in ESM A.

Furthermore, sensitivity tests for the description of free water transport are carried out to select the right approach. Two alternative formulations are analyzed namely concentration-based formulation and mixed formulation (Krabbenhøft 2004; Celia et al. 1990). The first approach uses a concentration-based formulation where the free water movement is described through a nonlinear diffusion equation:

$$\frac{\partial c_w}{\partial t} = \nabla \cdot (\mathbf{D}(c_w) \nabla c_w) \tag{17}$$

Here, $\mathbf{D}(c_w)$ represents the moisture-dependent diffusion tensor that accounts for the varying transport properties with water content. This formulation directly tracks the evolution of free water concentration and is particularly suitable for cases where concentration gradients drive the moisture movement.

The second approach employs a mixed formulation that combines both concentration and pressure-based components:

$$\frac{\partial c_w}{\partial t} = \nabla \cdot (\mathbf{K} \nabla P_c) \tag{18}$$

with the capillary pressure $P_c$ related to the saturation degree $S_w$ through an empirical relationship $P_c = 12400 S_w^{-0.61}$.

The numerical solution employs the finite element method with hexahedral elements and linear shape functions. The weak form of the governing equations (Eqs. (6)–(9)) leads to a coupled system of non-linear algebraic equations:

$$\begin{bmatrix} \frac{\partial F^M_{c_b}}{\partial c^Q_b} & \frac{\partial F^M_{c_b}}{\partial c^R_v} & \frac{\partial F^M_{c_b}}{\partial c^S_w} & \frac{\partial F^M_{c_b}}{\partial T^T} \\ \frac{\partial F^N_{c_v}}{\partial c^Q_b} & \frac{\partial F^N_{c_v}}{\partial c^R_v} & \frac{\partial F^N_{c_v}}{\partial c^S_w} & \frac{\partial F^N_{c_v}}{\partial T^T} \\ \frac{\partial F^O_{c_w}}{\partial c^Q_b} & \frac{\partial F^O_{c_w}}{\partial c^R_v} & \frac{\partial F^O_{c_w}}{\partial c^S_w} & \frac{\partial F^O_{c_w}}{\partial T^T} \\ \frac{\partial F^P_T}{\partial c^Q_b} & \frac{\partial F^P_T}{\partial c^R_v} & \frac{\partial F^P_T}{\partial c^S_w} & \frac{\partial F^P_T}{\partial T^T} \end{bmatrix} \cdot \begin{pmatrix} r^{c_b} \\ r^{c_v} \\ r^{c_w} \\ r^T \end{pmatrix} = \begin{pmatrix} -F^M \\ -F^N \\ -F^O \\ -F^P \end{pmatrix} \tag{19}$$

In this Eq. (19), the coefficient matrix (left-hand side) represents the partial derivatives of the residual functions $F^M_{c_b}$, $F^N_{c_v}$, $F^O_{c_w}$, and $F^P_T$ with respect to the nodal values $c^Q_b$, $c^R_v$, $c^S_w$, and $T^T$. The right-hand side contains the negative residuals, which drive the iterative solution process. The vector **r** contains the corrections to the nodal values, and the system is solved iteratively using a modified Newton method. To ensure accurate and stable numerical solutions, specific numerical techniques are employed. Upstream weighting (used to stabilize the convective terms in the transport equations) (Diersch and Perrochet 1999) and mass lumping (diagonalizing mass matrix) are used to address the non-linearity of the equations and ensure stability. These techniques help to improve the convergence of the solution and improves computational efficiency.

The model is implemented using hexahedral elements with linear shape functions via a UEL subroutine in the commercial finite element software Abaqus 2023. The implementation is done using the modified Newton method which is a robust iterative solver of Abaqus that can efficiently handle the non-linear system of equations arising from the model. Each element has 8 nodes, and each node has 4 degrees of freedom (DOFs): $c_b$, $c_v$, $c_w$, and $T$. These DOFs are represented by the Abaqus node labels NT11, NT12, NT13, and NT14, respectively. The field outputs are extracted for further analysis. The model utilizes a mesh with 4200 nodes. Python scripts are used to extract average node data and path data from the Abaqus output database (ODB) files. The implementation procedure, including the UEL flowchart, solution algorithm, and strategies for handling numerical challenges, is presented in ESM B.

## Model calibration

The numerical model was initially checked against two previously published datasets focusing on moisture transport below and above the FSP. First, the NMR-based data of Dvinskikh et al. (2011) served as a reference, demonstrating excellent agreement in the bound-water regime. Next, the numerical model was compared to the experiments of Gezici-Koç et al. (2017), which provided separate measurements of bound and free water fractions. Parameters from Autengruber et al. (2020) were used which resulted in reasonable agreement during the first 7 h of drying but showed different behaviour thereafter, as noted by Autengruber et al. (2020).

When these established parameter sets were applied to the present geometry, sorption isotherms, initial conditions, and boundary conditions, the numerical predictions deviated substantially from the corresponding CT data especially above the FSP. A targeted calibration was performed for the above-FSP regime, where

capillary and pressure-driven mechanisms govern free-water movement. This calibration included adjustments to the $\xi$-factor, $\mathbf{K_w}$ and $\mathbf{K_r}$ permeabilities, and the choice of free-water flow formulation (concentration-based vs. mixed concentration-pressure). the experiments were conducted at room temperature (23 °C), and no significant temperature gradients were introduced. Consequently, calibrating thermal conductivity did not yield additional information. Instead, Eq. A. 22 (see ESM A) was used to specify the thermal conductivity tensors, adopting an anisotropy ratio of 2:1:1 for the L, R and T-directions, respectively. This assignment aligns with commonly reported literature values for softwood species (Turner 1996).

In our current model, below the FSP, the model retained diffusion coefficients and reaction-kinetics parameters from Dvinskikh et al. (2011). Additional inputs, including $\rho_d$ (dry density), initial and boundary values for free-water concentration, and certain sorption-isotherm parameters, were derived from CT experiments. For the calibration process, three different literature-based $\mathbf{K_r}$ sets were used (Perré and Turner 1999; Sandoval-Torres et al. 2019), with $\xi$ and $\mathbf{K_w}$ varied within each set. Both the concentration-based (Eq. (17)) and the mixed concentration-pressure (Eq. (18)) formulations were examined. Simulations were then compared to CT-derived bound-water and free-water distributions over time.

## Results and discussions

### CT images at different cycles

The CT images of the SW wood sample taken along the L-direction (Fig. 5) illustrate the dynamic changes in MC within the wood sample during the drying process. Initially (0 h), the lumens are predominantly filled with free water, as evidenced by the high-intensity regions in the CT images. This observation aligns with the sample preparation, where the wood was submerged in water for 1–2 weeks to achieve full saturation, ensuring cell walls were filled with bound water and lumens contained free water, resulting in a high initial MC. The high intensity in the CT is due to the high attenuation coefficient of water as compared to air in the lumens.

After a few hours of drying, a noticeable reduction in free water content within the lumens is evident. The high-intensity regions representing free water become smaller and less frequent, indicating that a significant amount of free water has evaporated from the wood. This observation is consistent with the expected behaviour of wood during drying, where free water evaporates first due to its higher vapor pressure compared to bound water. The sealed lateral surfaces with heat shrink tubing, and top surfaces with PMMA plugs ensure that the moisture transport is occurring in the L-direction.

Already after a day, the lumens appear to be almost entirely devoid of free water. The CT images show a clear distinction between the cell walls, which retain some bound water, and the lumens, which are now filled with air. This observation suggests that the drying process has significantly progressed, and the wood sample is approaching its EMC at 65% RH.

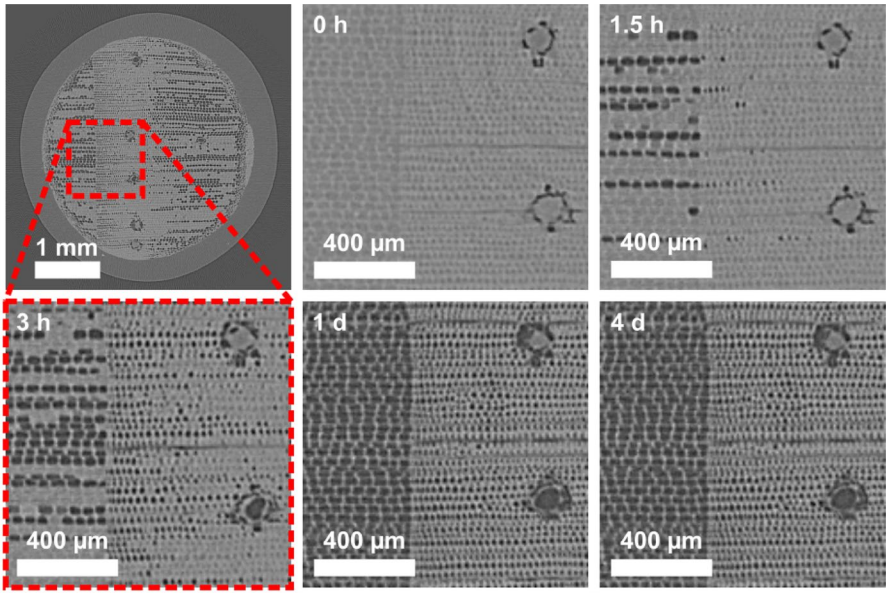


**Fig. 5** X-ray CT images of the longitudinal wood sample during the drying process. The first image (top left) shows the entire cross-section of a sample, and the other images show a zoomed area at different time points. All the slices are from the centre of the sample (z = 2.5 mm). The image sequence indicates a relatively rapid reduction of free water from the lumens

These observations highlight the effectiveness of the drying cycle facilitated by saturated salt solutions at room temperature. The images at 0 h confirm the initial conditions set for the model, where free water concentration $c_{w,ini}$ is non-zero. The observed decrease in free water content over time supports the boundary conditions and flux equations that account for the evaporation and transport of moisture.

## Numerical model calibration

Sorption isotherms for the numerical model were determined via DVS measurements (ESM C), which provided separate adsorption and desorption boundary curves to account for hysteresis within a state-based sorption model (see ESM A.4.1). Table 1 presents the shape parameters for the adsorption and desorption curves obtained at T = 25°C.

For calibration simulations, Scots pine SW properties in the L-direction were selected, aligning with the primary X-ray CT measurements. The initial free water MC was set to 94%, and the boundary conditions were applied to the bottom surface of the cylindrical sample using Eq. (A. 39) of ESM A, with an external RH of 33%, to simulate the drying process. Figure 6A and B illustrate the evolution of bound water and free water contents, respectively, over four days of drying, comparing

**Table 1** Shape parameters for the adsorption and desorption curves obtained from DVS measurements at T = 25°C

| Type | Adsorption | | | Desorption | | |
|---|---|---|---|---|---|---|
| | $f_{1a}$ (−) | $f_{2a}$ (−) | $f_{3a}$ (−) | $f_{1d}$ (−) | $f_{2d}$ (−) | $f_{3d}$ (−) |
| HW | 2.1655 | 13.87781 | −12.78066 | 1.92244 | 9.39717 | −8.05390 |
| SW | 2.09884 | 13.02058 | −11.88336 | 1.92297 | 8.55486 | −7.24176 |

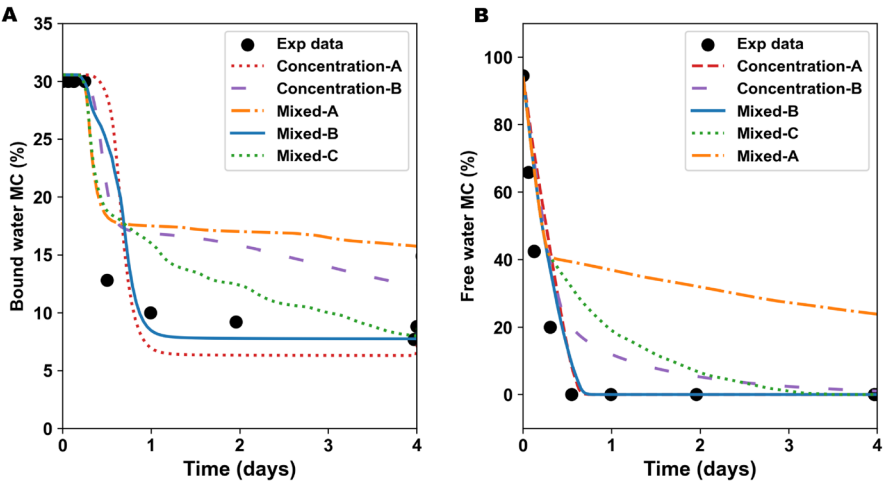


**Fig. 6** Comparison of experimental data with numerical model predictions. Average MC evolution during drying: (**A**) bound water MC; (**B**) free water MC. The plots compare experimental data (black circles) with predictions from five different numerical models: Concentration-A, Concentration-B, Mixed-A, Mixed-B, and Mixed-C

**Table 2** Model parameters for liquid permeability and $\xi$ factor in different directions

| Model type | Liquid permeability ($m^2$) | | | $\xi$ factor (−) | | |
|---|---|---|---|---|---|---|
| | L direction | R direction | T direction | L direction | R direction | T direction |
| Concentration-A | $1 \times 10^{-12}$ | $2 \times 10^{-15}$ | $1 \times 10^{-15}$ | 0.9 | 0.1 | 0.2 |
| Concentration-B | $1 \times 10^{-12}$ | $2 \times 10^{-15}$ | $1 \times 10^{-15}$ | 0.003 | 0.003 | 0.003 |
| Mixed-A | $5 \times 10^{-16}$ | $6 \times 10^{-19}$ | $5 \times 10^{-19}$ | 0.9 | 0.1 | 0.1 |
| Mixed-B | $1 \times 10^{-12}$ | $2 \times 10^{-15}$ | $1 \times 10^{-15}$ | 0.9 | 0.1 | 0.2 |
| Mixed-C | $1 \times 10^{-12}$ | $2 \times 10^{-15}$ | $1 \times 10^{-15}$ | 0.0003 | 0.0003 | 0.0003 |

Here $\mathbf{K_r}$ was set to $S_w^8$, $S_w^3$, $S_w^3$ in L, R and T-directions respectively

experimental CT data with five model variants labelled Concentration-A, Concentration-B, Mixed-A, Mixed-B, and Mixed-C. Table 2 provides the permeability values and $\xi$ factor settings for the models.

Figures 6A and 6B illustrate the evolution of bound water and free water contents, respectively, over four days of drying, comparing experimental CT data with five model variants: Concentration-A, Concentration-B, Mixed-A, Mixed-B, and Mixed-C. In the bound-water plot (Fig. 6A), both Concentration-A and Mixed-B capture the steep early drop in moisture content fairly well, but Concentration-A stabilizes at a lower bound-water level compared to the experiment. Mixed-A and Mixed-C remain higher than the experimental data beyond day one, indicating an underestimation of the bound-water desorption rate. Concentration-B falls somewhere in between, also overshooting the data after the first day.

A similar pattern emerges in the free-water content plot (Fig. 6B), where Concentration-A and Mixed-B again reproduce the rapid initial decline reasonably well, while Mixed-C and Concentration-B show a more gradual decrease. Notably, Mixed-A lags behind the experimental data, suggesting an overly slow free-water depletion. By contrast, Mixed-B aligns closely with the measurements throughout the entire four-day period. This strong fit is attributed to Mixed-B's ability to incorporate both concentration-driven and pressure-driven mechanisms at appropriate levels, complimented by a carefully calibrated $\xi$-factor that accounts for anisotropic vapor resistance. These features allow Mixed-B to replicate both the abrupt early-stage evaporative losses and the subsequent slower moisture-release phase observed in the CT data.

Overall, Mixed-B provides the best fit between capturing the rapid drop of free water in the first half-day and the more moderate drying rate thereafter. Concentration-based models (A and B) overemphasize diffusion at higher moisture contents or misrepresent capillary processes, leading to deviations from the measured free-water curve. For HW simulations, the same Mixed-B parameters are used, except that the $\xi$-factor in the tangential direction is set to 0.0003 (–).

### Moisture distribution along the longitudinal direction

The MC distribution along the longitudinal direction during drying and wetting cycles for the initial state (0 day), after 4 days, 8 days, and 12 days is shown in Fig. 7A, B and C. The figure presents the variations in bound water MC (Fig. 7A), free water MC (Fig. 7B), and total MC (Fig. 7C) from both experiments and numerical model B. For the numerical model, the average of paths along the longitudinal direction is considered.

The free water MC undergoes a rapid change during the initial stages of drying. At 0 days, the average free water content is 110%, indicating a high level of saturation within the wood's lumen. However, by the 4th day, the free water content drops to 0%, where it remains for the subsequent days (8th and 12th days). This sharp decline in free water content suggests that the initial drying phase at 33% RH effectively removes the free water, leaving the wood in a state where only bound water and water vapor remain.

The bound water MC shows a significant variation over time, reflecting the influence of the RH cycles. Initially, at 0 days, the bound water content is 32%, relatively uniform along the length of the sample. As drying progresses, the

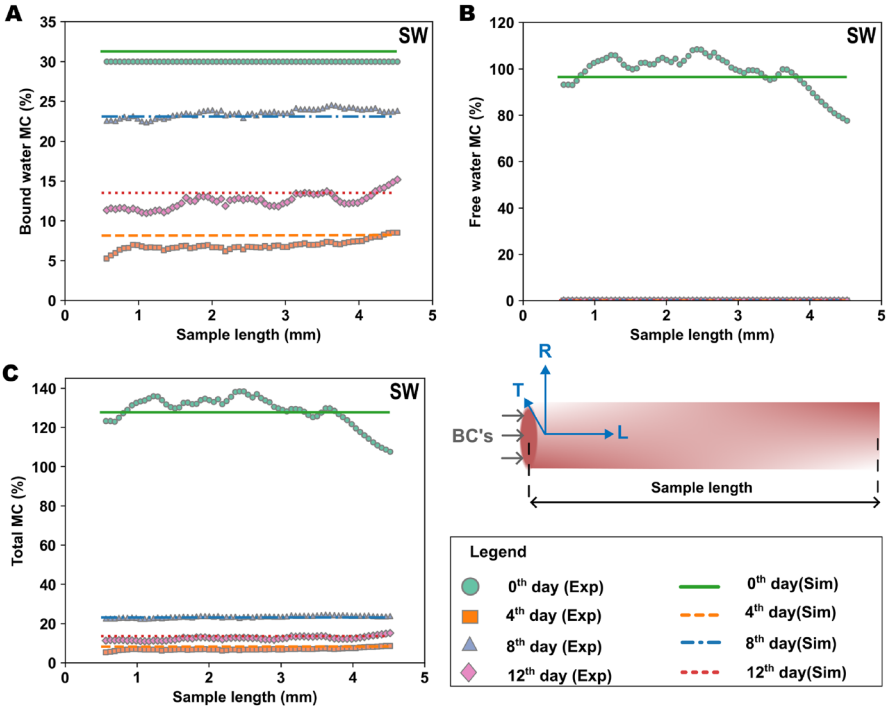


**Fig. 7** MC distribution along the longitudinal direction during drying and wetting cycles for the initial state (0 day), after 4 days, 8 days, and 12 days: **A** bound water MC; **B** free water MC; **C** total MC (sum of bound and free water). Here BCs refer to boundary conditions

bound water content decreases to 7% by the 4th day, indicating substantial moisture loss due to the initial drying phase at 33% RH. This reduction highlights the effectiveness of the initial drying conditions in removing bound water from the wood. However, as the RH increases to 94% and then to 64%, the bound water content increases again, reaching 14% at the 8th day and further rising to 23% at the 12th day.

The total MC, shown in Fig. 7C, is the sum of bound and free water contents as given in Eq. (1). Initially, the total MC is very high due to the substantial presence of both bound and free water. As drying progresses, the total MC decreases sharply to 7% by the $4^{th}$ day, primarily due to the loss of free water. At the $8^{th}$ day, the total MC increases to 14% and continues to rise to 23% by the $12^{th}$ day, reflecting the bound water content's increase due to the higher RH cycles. The predictions of the model align closely with the experimental data, confirming its capability to capture the overall moisture transport processes and the interactions between bound and free water.

These path plots reveal several key phenomena. The rapid decline of free water content during the initial drying phase emphasizes the efficiency of the drying process in removing free water from the wood's lumens. The stabilization of free

water content at 0% after the 4th day indicates that the remaining moisture is primarily bound water, which desorbs more slowly. This transition from free to bound water dominance is critical for understanding the drying kinetics of wood, particularly in applications where rapid moisture removal is desired. The bound water content decreases significantly during the initial drying phase at 33% RH, facilitating the desorption of bound water. As the RH increases to 94%, the wood reabsorbs moisture, leading to an increase of bound water content. This cyclic behaviour of desorption and absorption highlights the efficiency of the numerical model in capturing the hygroscopic nature of wood.

### Comparison of free and bound water MC along L, R and T directions

This section investigates the numerical results of the drying patterns of SW and HW under controlled conditions, focusing on both free water and bound water over time, over the first two days of drying at 33%, across the longitudinal, radial, and tangential directions of the wood. The color-coded contour plots shown in Fig. 8A–F provide a visual representation of these drying dynamics, helping to clarify the differences in MC across the wood's various directions.

In the L-direction, (composed of SW), free water undergoes a rapid decrease during the early stages of drying. This rapid reduction occurs due to the easier pathways for water movement along the wood grain, where the lumens facilitate swift evaporation under low RH conditions. The free water in the longitudinal direction is largely depleted within the first few hours, as reflected in the blues of the free water colormap plot (see Fig. 8A). As the intensity of the blues fades rapidly, it is clear that the lumina have emptied quickly, allowing bound water desorption. Bound water, however, follows a more gradual reduction after free water is near zero (see Fig. 8B). This slower decline can be observed in the greens of the bound water plot, where the color change indicates the desorption from the cell walls occurring only after the free water is removed.

In contrast, the R-direction (see Fig. 8C) and T-direction (see Fig. 8E) directions composed of HW, exhibit a more gradual moisture release. The free water in these directions shows a slower rate of decrease compared to the longitudinal direction, although the rate of free water removal in the radial and tangential directions is relatively similar. The colormap plots for free water in both directions depict a steady fading of blues (see Fig. 8C and E). The slower removal of free water in both radial and tangential directions reflects the increased resistance to moisture movement in HW.

For bound water, both R and T-directions demonstrate a delayed desorption compared to free water (see Fig. 8d and f). The greens in the bound water contour plots show a gradual transition as the bound water desorbs after the depletion of free water. The bound water in the T-direction shows slightly more resistance to desorption, with a slower color change compared to the radial direction, but the difference is not significant. Both directions require sustained drying conditions for meaningful reductions in bound water content, as indicated by the relatively stable green shades over extended drying periods.

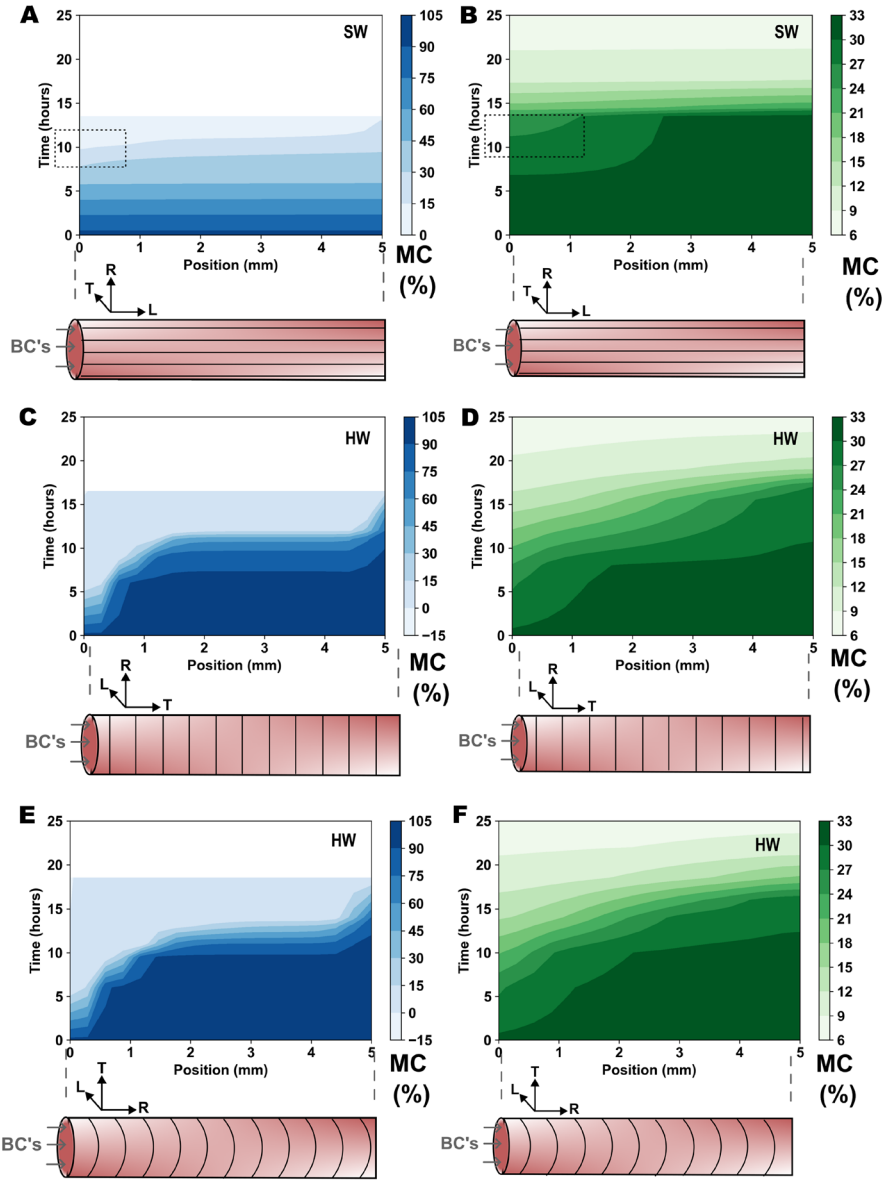


**Fig. 8** MC distribution along the different directions during drying cycles for the initial 2 days: **A** and **B** free water and bound water MC in longitudinal direction respectively; **C** and **D** free water and bound water MC in tangential direction respectively; **E** and **F** free water and bound water MC in radial direction respectively. Here BCs refer to boundary conditions

The numerical model underlying this analysis highlights the sequential nature of moisture release in wood. Free water must be nearly depleted at a given location before bound water desorption can occur. In the L-direction, this transition happens

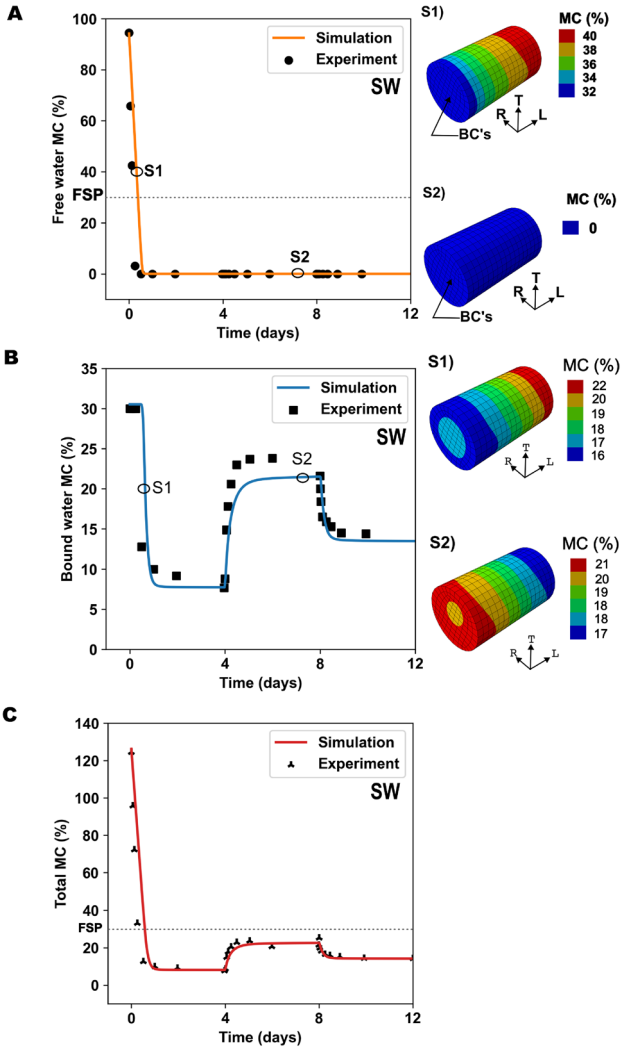


**Fig. 9** **A** Evolution of free water MC over time in the L-direction of wood, **B** evolution of bound water MC over time; **C** evolution of total MC over time. Markers S1 and S2 indicate specific time steps of FE simulation snippets showing MC distribution. Here BCs refer to boundary conditions

more quickly due to the rapid removal of free water. In the R and T-directions, the delayed depletion of free water leads to a later activation of bound water desorption.

## MC evolution over time

The evolution of average MC over time was monitored for bound water, free water, and total water in the wood samples (Fig. 9A, B and C). The figures present a

comparison between the experimental data and the numerical simulation results for the drying and wetting cycles.

The free water MC (Fig. 9A) exhibits a rapid decline from an initial high value of 110% to 0% by day 4, remaining at 0% thereafter. This sharp decrease reflects the efficient removal of free water from the wood's lumen under the initial drying conditions (33% RH). The numerical model accurately captures this rapid transition, validating its ability to simulate free water transport and evaporation dynamics. The bound water MC (Fig. 9B) initially decreases sharply from approximately 32% to around 7% by day 4 due to the low RH (33%) during the initial drying cycle. As the RH increases to 94% and then 64%, the bound water content rises, reaching 14% by day 8 and 23% by day 12, indicating the wood's reabsorption of moisture. The numerical model accurately simulates this dynamic behavior, capturing both the desorption and adsorption processes of bound water in response to varying RH.

The total MC is shown in Fig. 9C. It initially decreases sharply due to the loss of free water, reaching the 7% by day 4. Subsequently, it increases to 14% by day 8 and 23% by day 12, mirroring the rise in bound water content due to the higher RH cycles. The numerical model demonstrates good agreement with the experimental data, capturing the overall trend and variations in terms of total MC, thus confirming its robustness in simulating the combined effects of bound and free water transport, evaporation, and reabsorption.

### Radial and tangential directions

Figure 10A and B captures the distinct responses of SW in the R and T-directions to cycles of drying and wetting induced by changes RH. MC falls sharply from an initial 142% to 16%, a rapid drying reflecting the initial RH reduction to 33% (like the behaviour observed in L-direction). This quick drop to below the FSP suggests a pronounced susceptibility of the R-direction to external RH fluctuations.

In contrast, the T-direction, while following a broadly similar trend, shows a more moderated drying process during the same RH adjustments. The less pronounced drying rate in the T-direction may be indicative of its slower response to RH changes, a behavior that could be linked to its structural properties or the distribution of moisture pathways. As RH is subsequently increased to 94% and reduced again to 64%, both orientations show a stabilization of MC, yet the T-direction's slower response rate remains apparent.

### Additional insights and model usability

The parameterization of the proposed multi-phase moisture transport model relies on a combination of experimentally derived data and established literature-derived inputs. Key parameters such as sorption isotherms, diffusion tensors, permeability coefficients, and reaction rate constants have been prioritized based on their impact on model performance.

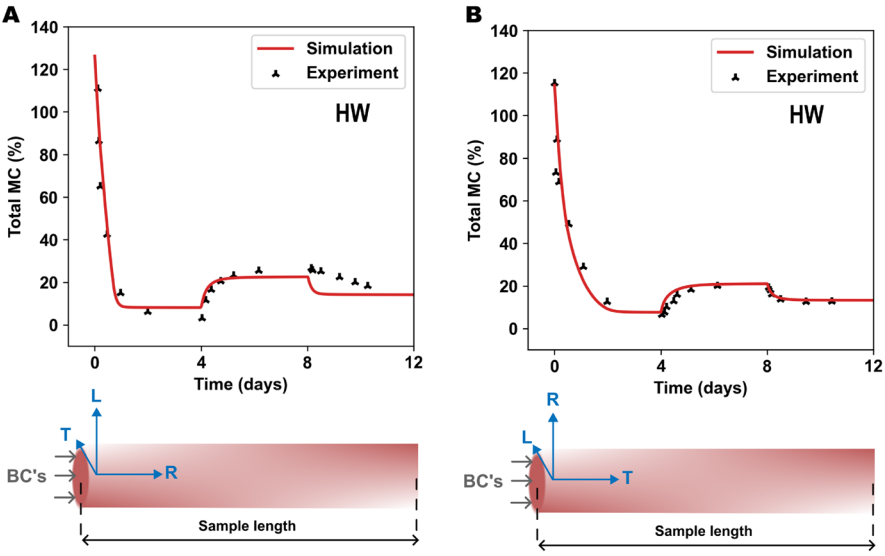


**Fig. 10** Evolution of total water MC over time in the: **A** radial direction of wood; **B** tangential direction of wood. Here BCs refer to boundary conditions

Sorption isotherms are foundational to understanding moisture adsorption and desorption behaviours, particularly for bound water evolution below FSP. These experiments, which involve controlled cycling of humidity, are well-suited for a variety of wood species and are supported by extensive prior studies (Frandsen et al. 2007a; Glass et al. 2018; Thybring and Fredriksson 2023). For new species, DVS experiments provide precise measurements of these behaviours under controlled humidity cycling. These will allow to determine the sorption hysteresis and moisture equilibrium states crucial for the model.

Diffusion tensors and permeability coefficients, essential for capturing both bound water and free water transport, can be quantified through steady-state and transient diffusion experiments. These properties are strongly influenced by wood's microstructure, which varies across species and even within SW and HW. Above the FSP, free-water flow dominates, and permeability tensors become crucial. Although wood permeability is often measured in specialized setups (Perre and Agoua 2010; Acosta et al. 2024), the natural variability of wood's microstructure-from sapwood to heartwood-requires careful calibration for different species or even different growth conditions. Reaction rate constants, which govern the interactions between bound water, free water, and vapor, are calibrated using experimental data and numerical fitting techniques. While prior studies such as Fortino et al. and Autengruber et al. have validated these constants in related contexts, they remain adaptable for different wood types (Dvinskikh et al. 2011; Fortino et al. 2019; Autengruber et al. 2020; Brandstätter et al. 2023).

A key advantage of X-ray CT lies in its ability to capture both macro- and microstructural information. Beyond quantifying moisture distribution, CT tomography provides detailed insights into microstructural features such as porosity, lumen

shape, and anisotropic pathways. Although the present study focuses on measuring moisture distributions rather than geometrical reconstruction, recent work by Zeng et al. demonstrates the use of CT data to construct full three-dimensional heterogeneous internal structure of wood with a novel FE tetrahedral mesh, enabling direct simulation of fluid pathways (Zeng et al. 2024). Such an approach could further refine free-water flow models or support investigations into fracture, swelling, and localized transport phenomena.

Despite its many benefits, CT remains nontrivial in cost and instrument availability. This can limit routine applications. Techniques such as NMR, offer a reliable alternative for characterizing bound and free water fractions (Gezici-Koç et al. 2017; El Hachem et al. 2020). Gravimetric moisture content measurements and steady-state diffusion tests can complement these approaches. However, for studies aiming to separate bound and free water behavior or needing spatially resolved information at high temporal resolution, CT proves uniquely valuable. In addition, CT remains important for advanced studies, such as those involving coupled processes like fungal decay, swelling, and anisotropic transport. For example, future extensions of this work using CT can be used to study the evolution of wood structure during decay and its impact on moisture transport pathways.

## Conclusions

This study presents a multi-phase model for moisture transport in Scots pine wood and evaluates its performance against high-resolution X-ray CT measurements obtained during alternating drying and wetting cycles. The model incorporates bound water, free water, and water vapor, treating their interactions with Fickian diffusion, Darcy's law, and phase-conversion processes. Anisotropic behavior in L, R and T-directions was also included to reflect the differing moisture responses of SW and HW above and below the FSP.

The CT images revealed the distinct behavior of free and bound water removal during drying, highlighting the fast evaporation of free water within lumens and the slower desorption of bound water from cell walls. Matching these measurements required careful calibration of non-trivial model parameters, including direction-dependent permeabilities, reduction factors for vapor diffusivity, and free-water formulations. Among the tested approaches, a mixed concentration-pressure formulation for free water flow-together with a calibrated direction-dependent vapor-diffusivity reduction factor-proved important for achieving high accuracy. The close agreement between simulated and experimental MCs indicates that high-resolution CT can effectively guide model parameter selection. Moreover, the model reproduced not only the overall drying kinetics but also subsequent reabsorption of moisture during higher RH phases.

These results confirm that the multi-phase model accurately captures both early free-water depletion and later bound-water fluctuations under different RH conditions, including variations along different anatomical directions in SW and HW. Integrating CT imaging into the calibration process was particularly beneficial in refining model accuracy, illustrating that a single modelling framework can account

for complex anisotropic moisture behavior. Future studies could extend these methods to include swelling or hygro-mechanical coupling, as well as investigate wood decay processes where multi-phase moisture behavior plays a key role.

**Supplementary Information** The online version contains supplementary material available at https://doi.org/10.1007/s00226-025-01635-9.

**Acknowledgements** The author would like to thank all researchers/scientists at VTT Technical Research Centre of Finland and the Institute of Mechanics of Materials and Structures, TU WIEN, who provided substantial contributions to the development of the user-element library for moisture transport in previous years.

**Author contributions** RDD: writing—original draft, visualization, software, investigation, methodology. TH and AM: investigation, methodology, writing - original draft, writing—review & editing, software. FB: investigation, writing—original draft, writing—review & editing, software. AN, MV and VM: investigation, writing—original draft, writing - review & editing. MB and AP: investigation, methodology, writing—original draft, writing—review & editing. JF: supervision, methodology, writing—review & editing, software. SF: supervision, methodology, writing—review & editing, software, funding acquisition, project administration.

**Funding** Open Access funding provided by Technical Research Centre of Finland. This research was funded by project "Image-based Modelling of Water Transport In Wood including material biodegradation - WaterInWood", Academy of Finland, Decision number 349194.

**Data Availability** No datasets were generated or analysed during the current study.

## Declarations

**Conflict of interest** The authors declare no competing interests.



## References

Acosta AP, de Avila Delucis R, Santos OL et al (2024) A review on wood permeability: influential factors and measurement technologies. J Indian Acad Wood Sci 21(1):175–191. https://doi.org/10.1007/s13196-024-00335-4

Almeida G, Gagné S, Hernández RE (2007) A NMR study of water distribution in hardwoods at several equilibrium moisture contents. Wood Sci Technol 41(4):293–307. https://doi.org/10.1007/s00226-006-0116-3

Autengruber M, Lukacevic M, Füssl J (2020) Finite-element-based moisture transport model for wood including free water above the fiber saturation point. Int J Heat Mass Transf 161:120228. https://doi.org/10.1016/j.ijheatmasstransfer.2020.120228

Belt T, Venäläinen M, Harju A (2021) Non-destructive measurement of Scots pine heartwood stilbene content and decay resistance by means of UV-excited fluorescence spectroscopy. Ind Crops Prod 164:113395. https://doi.org/10.1016/j.indcrop.2021.113395

Brandstätter F, Kalbe K, Autengruber M et al (2023) Numerical simulation of CLT moisture uptake and dry-out following water infiltration through end-grain surfaces. J Build Eng 80:108097. https://doi.org/10.1016/j.jobe.2023.108097

Cai C, Javed MA, Komulainen S et al (2020) Effect of natural weathering on water absorption and pore size distribution in thermally modified wood determined by nuclear magnetic resonance. Cellulose 27(8):4235–4247. https://doi.org/10.1007/s10570-020-03093-x

Celia MA, Bouloutas ET, Zarba RL (1990) A general mass-conservative numerical solution for the unsaturated flow equation. Water Resour Res 26(7):1483–1496. https://doi.org/10.1029/WR026i007p01483

Diersch HJG, Perrochet P (1999) On the primary variable switching technique for simulating unsaturated–saturated flows. Adv Water Resour 23(3):271–301. https://doi.org/10.1016/S0309-1708(98)00057-8

Dietsch P, Winter S (2018) Structural failure in large-span timber structures: A comprehensive analysis of 230 cases. Struct Saf 71:41–46. https://doi.org/10.1016/j.strusafe.2017.11.004

Dvinskikh SV, Henriksson M, Mendicino AL et al (2011) NMR imaging study and multi-Fickian numerical simulation of moisture transfer in Norway spruce samples. Eng Struct 33(11):3079–3086

Eitelberger J (2011) A multiscale material description for wood below the fiber saturation point with particular emphasis on wood-water interactions. Thesis, Technische Universität Wien, accepted: 2020-06-30T13:06:33Z Journal Abbreviation: Ein Mehrskalenmodell für Holz unter dem Fasersättigungspunkt unter besonderer Berücksichtigung der Wechselwirkungen zwischen Holz und Wasser

El Hachem C, Abahri K, Leclerc S et al (2020) NMR and XRD quantification of bound and free water interaction of spruce wood fibers. Constr Build Mater 260:120470. https://doi.org/10.1016/j.conbuildmat.2020.120470

Fortino S, Genoese A, Genoese A et al (2013) Numerical modelling of the hygro-thermal response of timber bridges during their service life: a monitoring case-study. Constr Build Mater 47:1225–1234. https://doi.org/10.1016/j.conbuildmat.2013.06.009

Fortino S, Hradil P, Genoese A et al (2019) Numerical hygro-thermal analysis of coated wooden bridge members exposed to Northern European climates. Constr Build Mater 208:492–505

Frandsen HL, Damkilde L, Svensson S (2007a) A revised multi-Fickian moisture transport model to describe non-Fickian effects in wood. Holzforschung, Walter de Gruyter 61(5):563–572. https://doi.org/10.1515/HF.2007.085

Frandsen HL, Svensson S, Damkilde L (2007b) A hysteresis model suitable for numerical simulation of moisture content in wood. Holzforschung, Walter de Gruyter 61(2):175–181. https://doi.org/10.1515/HF.2007.031,

Frandsen HL (2007) Selected constitutive models for simulating the hygromechanical response of wood. – Place: Aalborg Publisher: Department of Civil Engineering, Aalborg University

Gezici-Koç Ö, Erich SJF, Huinink HP et al (2017) Bound and free water distribution in wood during water uptake and drying as measured by 1D magnetic resonance imaging. Cellulose 24(2):535–553. https://doi.org/10.1007/s10570-016-1173-x

Glass SV, Boardman CR, Thybring EE et al (2018) Quantifying and reducing errors in equilibrium moisture content measurements with dynamic vapor sorption (DVS) experiments. Wood Sci Technol 52(4):909–927. https://doi.org/10.1007/s00226-018-1007-0

Harjupatana T, Alaraudanjoki J, Kataja M (2015) X-ray tomographic method for measuring three-dimensional deformation and water content distribution in swelling clays. Appl Clay Sci 114:386–394

Harjupatana T, Miettinen A, Kataja M (2022) A method for measuring wetting and swelling of bentonite using X-ray imaging. Appl Clay Sci 221:106485. https://doi.org/10.1016/j.clay.2022.106485

Konopka D, Kaliske M (2018) Transient multi-Fickian hygro-mechanical analysis of wood. Comput Struct 197:12–27. https://doi.org/10.1016/j.compstruc.2017.11.012

Krabbenhøft K (2004) Moisture transport in wood: a study of physical-mathematical models and their numerical implementation. BYG-Rapport, Technical University of Denmark, Kgs, Lyngby

Krabbenhoft K, Damkilde L (2004) A model for non-Fickian moisture transfer in wood. Mater Struct 37(9):615–622. https://doi.org/10.1007/BF02483291

Landis EN, Keane DT (2010) X-ray microtomography. Mater Charact 61(12):1305–1316. https://doi.org/10.1016/j.matchar.2010.09.012

Lehmann EH (2017) Neutron imaging facilities in a global context. J Imag 3(4):52. https://doi.org/10.3390/jimaging3040052

MacMillan B, Veliyulin E, Lamason C et al (2011) Quantitative magnetic resonance measurements of low moisture content wood1This article is a contribution to the series the role of sensors in the new

forest products industry and bioeconomy. Can J Forest Res 41(11):2158–2162. https://doi.org/10.1139/x11-081

Malo KA, Abrahamsen RB, Bjertnæs MA (2016) Some structural design issues of the 14-storey timber framed building "Treet'' in Norway. Eur J Wood Prod 74(3):407–424. https://doi.org/10.1007/s00107-016-1022-5

Miettinen A, Oikonomidis IV, Bonnin A et al (2019) NRStitcher: non-rigid stitching of terapixel-scale volumetric images. Bioinformatics 35(24):5290–5297. https://doi.org/10.1093/bioinformatics/btz423

Miettinen A, Harjupatana T, Kataja M et al (2016) Time-resolved X-ray microtomographic measurement of water transport in wood-fibre reinforced composite material. In: IOP conference series: materials science and engineering 139(1):012037. https://doi.org/10.1088/1757-899X/139/1/012037

Pang S (1998) Relative importance of vapour diffusion and convecttve flow in modelling of softwood drying. Dry Technol 16(1–2):271–281. https://doi.org/10.1080/07373939808917403

Perré P (2015) The proper use of mass diffusion equations in drying modeling: introducing the drying intensity number. Dry Technol 33(15–16):1949–1962. https://doi.org/10.1080/07373937.2015.1076836

Perre P, Agoua E (2010) Mass transfer in wood: identification of structural parameters from diffusivity and permeability measurements. J Porous Media 13(11):1017–1024. https://doi.org/10.1615/JPorMedia.v13.i11.80

Perré P, Turner IW (1999) A 3-D version of TransPore: a comprehensive heat and mass transfer computational model for simulating the drying of porous media. Int J Heat Mass Transf 42(24):4501–4521. https://doi.org/10.1016/S0017-9310(99)00098-8

Sandoval-Torres S, Pérez-Santiago A, Hernández-Bautista E (2019) Drying model for softwood and moisture patterns measured by magnetic resonance imaging. Dry Technol 37(4):458–467. https://doi.org/10.1080/07373937.2018.1457050

Stanish MA, Schajer GS, Kayihan F (1986) A mathematical model of drying for hygroscopic porous media. AIChE J 32(8):1301–1311. https://doi.org/10.1002/aic.690320808

Sterley M, Serrano E, Källander B (2021) 18 - Building and construction: timber engineering and wood-based products. In: Adams RD (ed) Adhesive bonding, 2nd edn. Woodhead Publishing, Darya Ganj, pp 571–603. https://doi.org/10.1016/B978-0-12-819954-1.00021-6

Thybring EE, Fredriksson M (2023) Wood and moisture. In: Niemz P, Teischinger A, Sandberg D (eds) Springer handbook of wood science and technology. Springer International Publishing, Cham, pp 355–397. https://doi.org/10.1007/978-3-030-81315-4_7

Thybring EE, Boardman CR, Zelinka SL et al (2021) Common sorption isotherm models are not physically valid for water in wood. Coll Surf A: Physicochem Eng Asp 627:127214. https://doi.org/10.1016/j.colsurfa.2021.127214

Thybring EE, Fredriksson M, Zelinka SL et al (2022) Water in wood: a review of current understanding and knowledge gaps. Forests 13(12):2051

Turner IW (1996) A two-dimensional orthotropic model for simulating wood drying processes. Appl Math Modell 20(1):60–81. https://doi.org/10.1016/0307-904X(95)00106-T

Turpeinen T, Myllys M, Kekäläinen P et al (2015) Interface detection using a quenched-noise version of the Edwards-Wilkinson equation. IEEE Trans Image Process 24(12):5696–5705. https://doi.org/10.1109/TIP.2015.2484061

Younsi R, Kocaefe D, Poncsak S et al (2006) Transient multiphase model for the high-temperature thermal treatment of wood. AIChE J 52(7):2340–2349. https://doi.org/10.1002/aic.10860

Zeng W, Fujimoto T, Inagaki T et al (2024) Three-dimensional modeling of moisture transport in wood using near-infrared hyperspectral imaging and X-ray computed tomography in conjunction with finite element analysis. J Wood Sci 70(1):9. https://doi.org/10.1186/s10086-023-02120-2

Žlahtič Zupanc M, Mikac U, Serša I et al (2019) Water distribution in wood after short term wetting. Cellulose 26(2):703–721. https://doi.org/10.1007/s10570-018-2102-y